

here include direct quantitative imaging of cyclic displacements as small as 100 nm, a freely oriented field of view unencumbered by the "acoustic window" required for ultrasound-based techniques, and the ability to study strain-wave propagation in a dynamic fashion. The flexibility of NMR methodology allows the motion-sensitizing gradient to be placed along any axis, so that with multiple acquisitions it is, in principle, feasible to estimate all components of the strain dyadic.

Two general fields of application for this technique are anticipated. The first is the study and visualization of strain-wave propagation within objects or materials that can be imaged with MRI. In principle, the method can depict the spatial patterns of wave propagation characteristics such as divergence, scatter, attenuation, interference, diffraction, and dispersion. If at least one full cycle of mechanical excitation is applied within the TE interval of the NMR sequence, then the practical low frequency limit is ~10 Hz. The upper frequency limit is determined by the maximum slew rate of the gradient system of the imager and is in the range of 1 to 2 kHz if the motion-sensitizing gradient oscillates at the same frequency as the mechanical excitation. Our experiments have shown that we can image mechanical-excitation wave forms ranging from continuous waves to repeated short wave trains or even single cycles of mechanical excitation repeated each TR cycle.

A second general area of application is to apply mechanical strain wave excitation to interrogate the properties of materials within a heterogeneous object. Elastic moduli are of special interest in the context of medical applications. For centuries, physicians have used palpation of the body to detect the presence of tumors and other diseases. Unfortunately, many structures of the body are not accessible to the palpating hand. It is not unusual at the time of abdominal laparotomy for surgeons to discover tumors by direct palpation of abdominal organs that have gone undetected in prior imaging by computed tomography, ultrasound, or conventional MRI. In addition to potentially providing a noninvasive "palpation" technique that extends the reach and resolution of the diagnostic method, MRE offers the possibility of providing other measurable viscoelastic parameters such as attenuation and dispersion as criteria for further tissue characterization. We speculate that MRE may have a role in the detection of tumors of the breast, liver, kidney, and prostate.

REFERENCES AND NOTES

1. H. Kolsky, *Stress Waves in Solids* (Dover, New York, ed. 1, 1963), pp.131-168.  
 2. E. L. Hahn, *J. Geophys. Res.* **65**, 776 (1960).

3. The first gradient moment is defined as  $\int_0^T \mathbf{G}_x(t) dt$ , where  $\mathbf{G}_x(t) = G_x \hat{i} + G_y \hat{j} + G_z \hat{k}$ .  
 4. P. R. Moran, *Magn. Reson. Imaging* **1**, 197 (1982).  
 5. P. van Dijk, *J. Comput. Assist. Tomogr.* **8**, 429 (1984).  
 6. D. J. Bryant *et al.*, *ibid.*, p. 588.  
 7. L. R. Pelc *et al.*, *Radiology* **185**, 809 (1992).  
 8. The applied switching polarity gradient is given by

$$\mathbf{G}_x(t) = \begin{cases} + |G| & \text{for } (n-1)T < \tau < (2n-1)T/2 \\ - |G| & \text{for } (2n-1)T/2 < \tau < nT \end{cases}$$

where  $n = 1, 2, \dots, N$  and  $\tau = NT$ .  
 9. 1.5-T General Electric Medical Systems Signa; Milwaukee, WI.  
 10. A. Kumar, D. Welte, R. R. Ernst, *J. Magn. Reson.* **18**, 69 (1975).  
 11. The pulse sequence is performed twice for each phase-encoding view with motion-sensitizing gradients of opposite polarity. The two reconstructed data sets are subtracted to yield phase-difference images, analogous to methods used for phase-contrast MR angiography (12, 13).  
 12. C. L. Dumoulin and H. R. Hart, *Radiology* **161**, 717 (1986).  
 13. N. J. Pelc, M. A. Bernstein, A. Shimakawa, G. H. Glover, *J. Magn. Reson. Imaging* **1**, 405 (1991).  
 14. The displacement at the driving surface was measured by observing the deflection of a laser beam

reflected from a mirror attached to the pivoting mechanical actuator.  
 15. H. Knutsson, C. J. Westin, G. Granland, *Proceedings of the IEEE International Conference on Image Processing-94* (IEEE Computer Society Press, Los Alamitos, CA, ed. 1, 1994), p. 36.  
 16. M. M. Burlew *et al.*, *Radiology* **134**, 517 (1980).  
 17. K. J. Parker, S. R. Huang, R. A. Musulin, R. M. Lerner, *Ultrasound Med. Biol.* **16**, 241 (1990).  
 18. S. R. Huang, thesis, University of Rochester, Rochester, NY (1990).  
 19. J. Ophir, I. Cespedes, H. Ponnekanti, Y. Yazdi, X. Li, *Ultrasound Imaging* **13**, 111 (1991).  
 20. D. B. Plewes, I. Betty, I. Soutar, *Proc. Soc. Magn. Reson.* **1**, 410 (1994).  
 21. C. J. Lewa and J. D. de Certaines, *J. Magn. Reson. Imaging* **5**, 241 (1995).  
 22. For purposes of testing, a Poisson ratio of 0.495 was assumed.  
 23. Y. C. Fung, *Biomechanics: Mechanical Properties of Living Tissues* (Springer-Verlag, New York, ed. 1, 1981), pp. 35-38.  
 24. E. L. Madsen, H. J. Sathoff, J. A. Zagzebski, *J. Acoust. Soc. Am.* **74**, 1346 (1983).  
 25. We gratefully acknowledge the contributions of S. J. Riederer, K. N. An, and J. J. Grabowski to this work. Partially supported by NIH grant CA51124.

24 April 1995; accepted 20 July 1995

## Anisotropy and Spiral Organizing Centers in Patterned Excitable Media

Oliver Steinbock, Petteri Kettunen, Kenneth Showalter\*

Chemical wave behavior in a patterned Belousov-Zhabotinsky system prepared by printing the catalyst of the reaction on membranes with an ink jet printer is described. Cellular inhomogeneities give rise to global anisotropy in wave propagation, with specific local patterns resulting in hexagonal, diamond, and pentagonal geometries. Spiral wave sources appear spontaneously and serve as organizing centers of the surrounding wave activity. The experimental methodology offers flexibility for studies of excitable media with made-to-order spatial inhomogeneities.

Propagating waves are observed in living organisms and biological tissues (1) as well as excitable chemical systems (2). The familiar rotating spiral waves and expanding target patterns of the Belousov-Zhabotinsky (BZ) reaction (3) are also observed in thin slices of heart tissue (4), in the cytoplasm of frog oocytes (5), and in animal retinas (6). Three-dimensional scroll waves, extensively studied in the BZ reaction (7), have now been characterized in migrating slugs of the slime mold *Dictyostelium discoideum* (8), and it is likely that these waves are precursors to ventricular fibrillation in mammals (9). The cellular nature of living systems, however, gives rise to inhomogeneities and anisotropy not present in homogeneous reaction systems, and these may play an important role in the behavior of biological media. A crucial example is found in the anisotropy of mammalian heart muscle

(10). The cellular structure of cardiac tissue not only causes local variations in wave velocity (4) but also gives rise to propagation failure (11). In this report, we describe wave behavior in excitable media with well-defined cellular inhomogeneities obtained by printing catalyst patterns on a BZ-membrane system. Our experimental and numerical investigations show that local patterns determine the global wave geometry and give rise to spontaneous organizing centers.

Noszticzus and co-workers (12) have recently demonstrated that bathoferroin, a catalyst and indicator for the BZ reaction (13), is effectively immobilized on polysulfone membranes. Our experimental method is based on the precision loading of this catalyst onto the membranes with an ink jet printer (14). Patterns were generated as black and white images by a commercial graphics program, which were then printed with the catalyst solution on the polysulfone membranes. Following Noszticzus (12), the ready-to-use membranes were

Department of Chemistry, West Virginia University, Morgantown, WV 26506-6045, USA.

\*To whom correspondence should be addressed.

placed on agarose gels containing BZ solution (15), which provided a continuous supply of reactants to the catalyst-loaded regions without hydrodynamic disturbances of the wave activity. The wave behavior was monitored by measuring the reflected

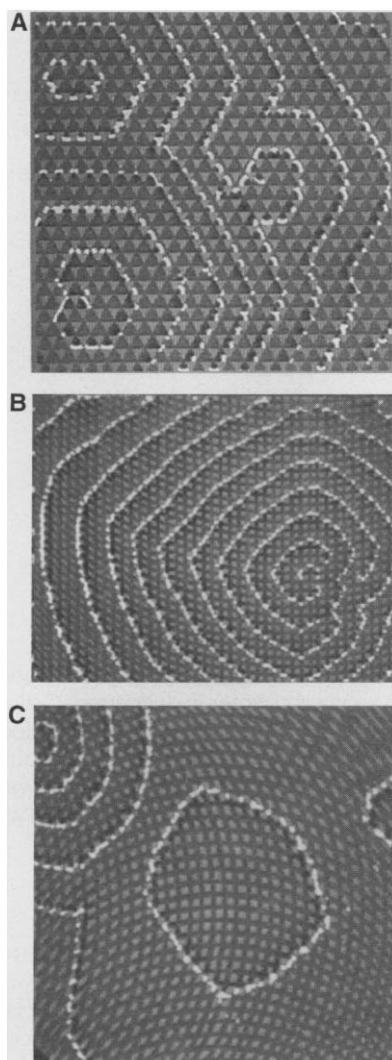


**Fig. 1.** Propagating waves on BZ membranes with cellular inhomogeneities. Catalyst patterns appear as the background in each figure; unloaded and loaded regions are light and dark gray, respectively: **(A)** Triangular cells of side length 1.65 mm; **(B)** superimposed linear and circular grids ( $\sim 1$  vertical line per millimeter; the radius of vertically shifted circle segments is  $\sim 4$  cm); **(C)** superimposed circular grids (radius of circle segments is  $\sim 2.1$  cm with a horizontal and vertical shift of  $\sim 1$  curve/mm). The specific catalyst patterns gave rise to **(A)** hexagonal, **(B)** diamond-shaped, and **(C)** pentagonal wave patterns. Image areas are **(A)** 14.5 cm<sup>2</sup>, **(B)** 13.5 cm<sup>2</sup>, and **(C)** 8.4 cm<sup>2</sup>. Line thickness in **(B)** and **(C)** was 0.33 mm. The positions of the waves, obtained by subtraction of successive video frames, were superimposed on the background image, with white assigned to the wave front and black assigned to the wave back. Spiral waves in **(A)** and **(B)** occurred spontaneously, whereas the wave in **(C)** was initiated by contacting the membrane with a silver wire.

light (wavelength  $\lambda = 500$  nm) from the medium with a charge-coupled device (CCD) video camera.

Wave propagation was studied on various catalyst-loaded membranes, each printed with a different pattern. A checkerboard arrangement of triangular cells gave rise to hexagonal wave geometry (Fig. 1A). Similarly, diamond-shaped wave structures developed on cross-hatched linear grids, and deformations of higher complexity occurred on less symmetrical patterns. A nonlinear catalyst grid of superimposed parallel lines and vertically shifted circle segments (Fig. 1B) gave rise to a distorted diamond geometry with the left corner following a specific arc. Video frame sequences demonstrated that the spiral tips in Fig. 1, A and B, rotated around particular catalyst-free cells on the membrane, effectively pinning the spiral waves. A similar pinning of spiral waves in heart tissue to anatomical discontinuities such as small arteries has been reported (4).

Wave patterns with approximately five-fold symmetry may occur in catalyst grids consisting of superimposed arrays of shifted circular arcs (Fig. 1C). The pentagonal shape has four prominent corners that coincide with two catalyst-loaded arcs. The intersection of these arcs is close to the point of wave initiation. The fifth, somewhat smoother corner is directed along the unique symmetry axis of the catalyst pattern (toward the upper right).

We carried out numerical simulations of the wave behavior using the Tyson-Fife model (16, 17) of the BZ reaction, modified to reflect the features of the patterned medium. The model has the form

$$\frac{\partial u}{\partial t} = \nabla^2 u + f(u, v) \quad (1)$$

$$\frac{\partial v}{\partial t} = g(u, v) \quad (2)$$

where the variables  $u$  and  $v$  describe the scaled concentrations of the propagator species  $\text{HBrO}_2$  and the controller species bathoferriin, respectively. Catalyst-free regions on the membrane were modeled by omitting the equation for  $v$  and all terms in  $f(u, v)$  that involve the catalyst (17). This allows the propagator species  $u$  to penetrate catalyst-free regions even though these areas do not support active wave propagation.

While the experimental measurements yield information about the wave propagation based on the bathoferriin concentration, the numerical simulations can provide insights in terms of the autocatalytic species  $\text{HBrO}_2$ . A grid of triangular cells (Fig. 2A) gives rise to a hexagonal wave pattern much like the experimentally measured waves (Fig. 1A). As in the experiment, the rotating spiral tips are pinned to specific catalyst-free cells. The pentagonal wave arising from a grid of superimposed arrays of shifted circular arcs (Fig. 2B) is also in good agreement with the corresponding experimental wave pattern (Fig. 1C). Elevated levels of  $u$  appear in catalyst-free cells behind the waves in both simulations (Fig. 2). These islands of autocatalyst are not able to initiate additional waves, however, because they are surrounded by catalyst-loaded cells in the refractory state (18). It is possible that such regions of elevated  $u$  are relevant to the appearance of “echo waves” in the trailing edge of a wave, a phenomenon observed in heart tissue (19).

The wave patterns in Figs. 1 and 2 can be understood in terms of a simple geometric mechanism. Assuming the catalyst-free cells to be impenetrable obstacles, the geometries

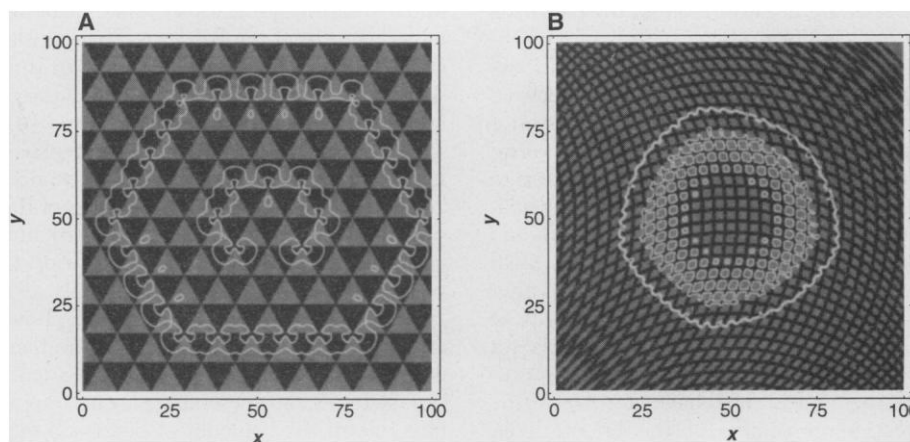


**Fig. 2.** Two-dimensional simulations of wave patterns. Black and gray areas indicate catalyst-loaded and catalyst-free regions, respectively. Superimposed white curves represent contour lines of the variable  $u$  at a given time. **(A)** Spiral pair forming hexagonal pattern (contour line at half-maximum of the propagator variable,  $u_{\max}/2$ ); **(B)** wave with pentagonal deformation (contour lines at  $u_{\max}/3$  and  $2u_{\max}/3$ ). Equations were integrated on a grid of  $300 \times 300$  points (grid spacing  $\Delta x = 1/3$ ; time step  $\Delta t = 0.001$ ) with  $f = 2.5$  for excitable kinetics (17).

can be deduced by determining paths along the catalyst-loaded cells of equal distance from the wave origin. Waves propagating along continuous lines of the catalyst grid therefore form corners of the pattern, and the most circuitous routes form the least advanced edges. In addition, the diffusion of  $\text{HBrO}_2$  into the catalyst-free cells and its flux into neighboring catalyst-loaded cells provide a mechanism for wave transmission across the barriers. In experiments with catalyst-loaded squares separated by catalyst-free strips, continuous wave patterns formed across the array despite the unexcitable barriers (20). The extent of wave transmission across the catalyst-free regions depended on excitability and barrier width, with the corresponding wave geometries ranging from sharply polygonal to the familiar circles and spirals of homogeneous media.

Experiments were carried out to examine wave behavior in media containing random heterogeneities (Fig. 3A). Patterns were printed with a catalyst dot density linearly increasing from 0.1 to 1.0. The dot

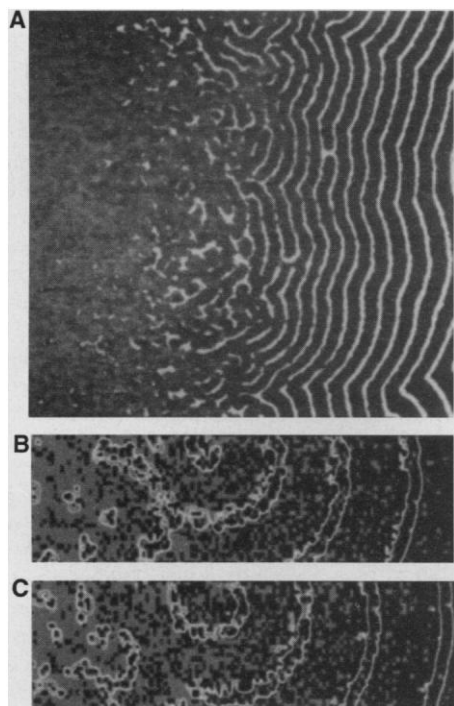


**Fig. 3.** Chemical waves on a linear dot density gradient with random dot locations perpendicular to the gradient. **(A)** Wave behavior on catalyst-loaded membrane; wave positions (white) obtained by image subtraction ( $\Delta t = 6$  s). The density of catalyst-loaded dots varies from 0.1 (left) to 1.0 (right); field of view,  $9.7 \text{ cm}^2$ . **(B and C)** Numerical simulations of wave behavior: two successive images with  $\Delta t = 2$ . Wave patterns, indicated by white contour lines of the variable  $u$  (as in Fig. 2B), evolved slowly from uniform initial conditions. Dot density varies linearly from 0.1 (left) to 0.9 (right). Parameters of simulation:  $600 \times 150$  grid points, grid spacing  $\Delta x = 1/3$ , time step  $\Delta t = 0.001$ , and  $f = 1.25$  for oscillatory kinetics (17).

density was equally incremented each printed line for 300 lines, with the dots in each line placed according to a random number generator. The random heterogeneities were on a much finer scale than the patterns described above because they occurred dot-wise, close to the resolution of the printer. On the left side of the membrane (Fig. 3A), the dot density is insufficient to support wave activity. Irregular waves are exhibited between a density of about 0.3 and 0.5, below which only fleeting spots of excitation are found. The waves become regular at a dot density greater than about 0.6. Qualitatively similar behavior was found with reactant solutions of lower excitability (containing a lower sulfuric acid concentration), where the transition from irregular to regular behavior occurred at higher dot density. The wave segments in regions of intermediate dot density tended to serve as high-frequency sources, eventually entraining the behavior in the higher density regions. This entrainment resulted in overall wave propagation from regions of low dot density to high dot density (from left to right in Fig. 3).

Figure 3, B and C, shows successive images of the simulated behavior, with regions of elevated  $u$  within the contour curves (21). At very low dot density, regions of excitation appear but are ineffective in initiating waves. At an intermediate dot density between 0.3 and 0.4, larger regions of excitation form broken wave segments that serve as wave sources as they undergo spiral-like rotation. Waves also emanate from symmetrical pacemakers in this region. The waves become regular as they move into regions of higher dot density. While the intermediate level heterogeneity gives rise to organizing wave centers, the waves in regions of higher dot density are remarkably unaffected by the heterogeneity.

Spiral waves do not occur spontaneously in homogeneous media. In homogeneous BZ systems, they form at either physically or chemically induced wave breaks (1, 3). Special initial conditions, such as cross-field stimulation (4, 22) or wave initiation in the vulnerable region of a preceding wave (23) can also give rise to spiral waves. In biological excitable media, however, spiral waves appear spontaneously without special initial conditions or induced wave breaks. The most common explanation for their occurrence involves the heterogeneity in refractoriness of the medium (24), although it is now known that impenetrable obstacles may also lead to spiral wave formation (25).

Spiral waves and rotating wave segments also arise in heterogeneous systems from the interaction of cells or clusters of cells with different oscillatory frequencies. The experiment and simulation shown in Fig. 3 uti-

lized oscillatory media, initially homogeneous throughout the system. Each catalyst pattern exhibited bulk oscillations, with spurious wave initiations occurring at higher frequency sites, which were located in the smaller catalyst regions and at the catalyst boundaries. The resulting loss of synchronization gave rise to the rotating wave sources shown in the experimental and calculated images (26). Several mechanisms could give rise to spiral waves in such asynchronous oscillatory media, for example, wave initiation in the vulnerable region of a precursor wave. The spiral waves in Fig. 1, A and B, also appeared spontaneously, and such spiral organizing centers were common in all the patterned media. Spiral centers form spontaneously in other cellular media, including the slime mold *D. discoideum* (8) and a catalyst-bead BZ system (27).

Polygonal wave patterns have also been observed in the reaction of  $\text{NO} + \text{H}_2$  on Rh(110), where state-dependent diffusion anisotropy gives rise to wave deformations (28). Elliptical waves are observed in heart tissue as a result of different propagation velocities along the long axis of the cells and in the transverse direction (4). The printed BZ-membrane system, with well-defined and easily varied catalyst patterns, offers a convenient and versatile system for the study of anisotropy and cellular inhomogeneities in excitable media. Our study has shown that inhomogeneities on small length scales strongly influence global wave behavior, giving rise to patterns with pronounced anisotropy as well as spontaneous spiral wave sources. Such effects are undoubtedly present in the cellular media of excitable biological systems.

## REFERENCES AND NOTES

1. J. D. Murray, *Mathematical Biology* (Springer, Berlin, 1989); A. T. Winfree, *When Time Breaks Down* (Princeton Univ. Press, Princeton, NJ, 1987).
2. R. J. Field and M. Burger, Eds., *Oscillations and Traveling Waves in Chemical Systems* (Wiley, New York, 1985); R. Kapral and K. Showalter, Eds., *Chemical Waves and Patterns* (Kluwer, Dordrecht, Netherlands, 1995); S. K. Scott, *Oscillations, Waves, and Chaos in Chemical Kinetics* (Oxford Univ. Press, Oxford, 1994).
3. A. N. Zaikin and A. M. Zhabotinsky, *Nature* **225**, 535 (1970); A. T. Winfree, *Science* **175**, 634 (1972).
4. J. M. Davidenko et al., *Nature* **355**, 349 (1992).
5. J. Lechleiter, S. Girard, E. Peralta, D. Clapham, *Science* **252**, 123 (1991).
6. A. Gorelova and J. Bures, *J. Neurobiol.* **14**, 353 (1983).
7. A. T. Winfree, *The Geometry of Biological Time* (Springer, Berlin, 1980); B. J. Welsh et al., *Nature* **304**, 611 (1983); A. T. Winfree, *Chaos* **1**, 303 (1991).
8. O. Steinbock, F. Siegert, S. C. Müller, C. J. Weijer, *Proc. Natl. Acad. Sci. U.S.A.* **90**, 7332 (1993).
9. A. T. Winfree, *Science* **266**, 1003 (1994); N. Wiener and A. Rosenblueth, *Arch. Inst. Cardiol. Mex.* **16**, 205 (1946).
10. L. Clerc, *J. Physiol. (London)* **255**, 335 (1976); J. P. Keener, *J. Math. Biol.* **29**, 629 (1991); A. V. Panfilov and J. P. Keener, *Int. J. Bifurcation Chaos* **3**, 445 (1993); P. M. F. Nielsen et al., *Am. J. Physiol.* **260**, H1365 (1991).

# Replicator Neural Networks for Universal Optimal Source Coding

Robert Hecht-Nielsen

11. M. Delmar *et al.*, *Circ. Res.* **60**, 780 (1987).
12. A. Lázár, Z. Noszticzius, H. Farkas, H.-D. Försterling, *Chaos* **5**, 443 (1995); A. Lázár, Z. Noszticzius, H.-D. Försterling, Zs. Nagy-Ungvárai, *Physica D* **84**, 112 (1995).
13. T. Yamaguchi, L. Kuhnert, Zs. Nagy-Ungvárai, S. C. Müller, B. Hess, *J. Phys. Chem.* **95**, 5831 (1991).
14. Solutions of the catalyst  $\text{Fe}(\text{batho})_3^{2+}$  were prepared by dissolving 50.0 mg of 4,7-diphenyl-1,10-phenanthroline (known as bathophenanthroline) and 31.4 mg of  $\text{FeSO}_4 \cdot 7 \text{H}_2\text{O}$  in 10.0 ml of glacial acetic acid. Approximately 5 ml of the filtered catalyst solution (filter pore size, 0.45  $\mu\text{m}$ ) were pipetted into a clean, dry printer cartridge (HP51626A), which was resealed. The cartridge was used with a Hewlett Packard DeskJet 520 to print the catalyst patterns onto the polysulphone membranes (Gelman Supor-450).
15. The gel was prepared by mixing 10 ml of liquid agar (Agar-Agar; Fluka, New York) with 10 ml of BZ solution (without catalyst) in a thermostated Petri dish (diameter, 8.5 cm) maintained at  $25.0 \pm 0.2^\circ\text{C}$ . Resulting initial composition: 1.5% agar,  $[\text{NaBrO}_3] = 0.26 \text{ M}$ ,  $[\text{malonic acid}] = 0.17 \text{ M}$ ,  $[\text{NaBr}] = 0.10 \text{ M}$ , and  $[\text{H}_2\text{SO}_4] = 0.31 \text{ M}$  (Fig. 1) or 0.39 M (Fig. 3).
16. J. J. Tyson and P. C. Fife, *J. Chem. Phys.* **73**, 2224 (1980); J. P. Keener and J. J. Tyson, *Physica D* **21**, 307 (1986).
17. Functions  $f$  and  $g$  for the catalyst-loaded areas are defined as  $f(u, v) = (1/\epsilon)[u - u^2 - \epsilon v(u - q)/(u + q)]$  and  $g(u, v) = u - v$ . Catalyst-free regions were described by Eq. 1 with  $f(u, v) = (1/\epsilon)(-u^2)$ . The Laplacian was approximated by a nine-point formula; parameters:  $\epsilon = 0.05$  and  $q = 0.002$ .
18. The retarded decay of  $\text{HBrO}_2$  in catalyst-free regions is an intrinsic feature of the model and is consistent with the Field-Körös-Noyes mechanism of the BZ reaction [R. J. Field, E. Körös, R. M. Noyes, *J. Am. Chem. Soc.* **94**, 8649 (1972)]. It reflects the absence of the catalyzed production of the inhibitor bromide in these regions. One-dimensional simulations with the three-variable Oregonator model [R. J. Field and R. M. Noyes, *J. Chem. Phys.* **60**, 1877 (1974)] showed the same qualitative behavior.
19. J. Jalife, *Pacing Clin. Electrophysiol.* **6**, 1106 (1983).
20. The catalyst-free strips were 0.5 mm in width and the experimental conditions were the same as in Fig. 1 except  $[\text{H}_2\text{SO}_4] = 0.39 \text{ M}$ . Gap penetration by BZ waves has also been observed in an immobilized-catalyst sol-gel system [I. R. Epstein, I. Lengyel, S. Kádár, M. Kagan, M. Yokoyama, *Physica A* **188**, 26 (1992)].
21. The length scale for the calculation corresponds to an approximately threefold enlargement except for the dot-density gradient. This scale was required to achieve sufficient accuracy in feasible computational times. The number of dots per wavelength in simulation and experiment is approximately the same.
22. A. T. Winfree, *J. Theor. Biol.* **138**, 353 (1989).
23. M. Gómez-Gesteira *et al.*, *Physica D* **76**, 359 (1994).
24. G. K. Moe, W. C. Rheinboldt, J. A. Abildskov, *Am. Heart J.* **67**, 200 (1964).
25. K. Agladze *et al.*, *Science* **264**, 1746 (1994); M. Gómez-Gesteira *et al.*, *Phys. Rev. E* **50**, 4646 (1994); A. Babloyantz and J. A. Sepulchre, *Physica D* **49**, 52 (1991); J. A. Sepulchre and A. Babloyantz, in *Chemical Waves and Patterns*, R. Kapral and K. Showalter, Eds. (Kluwer, Dordrecht, Netherlands, 1995), pp. 191-217.
26. The experimental system (Fig. 3A) evolved to the asymptotic behavior in only a few oscillations, whereas the simulated system (Fig. 3, B and C) required many cycles; this difference is likely the result of a greater role played by external fluctuations and imperfections in the experimental system.
27. J. Maselko and K. Showalter, *Physica D* **49**, 21 (1991).
28. F. Mertens and R. Imbühl, *Nature* **370**, 124 (1994).
29. We thank Z. Noszticzius and V. Gáspár for advice on loading polysulphone membranes with bathoferroin. We are grateful to the National Science Foundation (CHE-9222616), the Office of Naval Research (N00014-95-1-0247), and the Petroleum Research Fund (29565-AC6) for supporting this research. O.S. thanks the Fonds der Chemischen Industrie for a Liebig Fellowship.

22 May 1995; accepted 10 July 1995

Replicator neural networks self-organize by using their inputs as desired outputs; they internally form a compressed representation for the input data. A theorem shows that a class of replicator networks can, through the minimization of mean squared reconstruction error (for instance, by training on raw data examples), carry out optimal data compression for arbitrary data vector sources. Data manifolds, a new general model of data sources, are then introduced and a second theorem shows that, in a practically important limiting case, optimal-compression replicator networks operate by creating an essentially unique natural coordinate system for the manifold.

The first serious studies of replicator neural networks were carried out by Kohonen (1) during the 1970s. Ackley, Hinton, and Sejnowski (2) later considered the "encoder problem" for Boltzmann machines. In 1986, Cottrell, Munro, and Zipser (3) developed a replicator network version of the multilayer perceptron neural network (4). This report focuses on a three hidden layer version of this last architecture. In the following, a data vector is defined as a point  $\mathbf{x} = (x_1, x_2, \dots, x_m)$  in  $\mathfrak{R}^m$  (for example, the brightnesses of pixels in an  $m$ -pixel image tile or  $m$  regular time samples of a sound stream). A source is a statistical process that supplies data vectors that belong to a compact measurable subset  $A$  of  $\mathfrak{R}^m$ , where the a priori probability of a data vector  $\mathbf{x}$  being supplied is governed by a regular probability distribution  $\mu$  (5) on  $\mathfrak{R}^m$  with  $\mu(A) = 1$  (a distribution defined on  $A$ ). The case where  $m$  is large (say,  $m > 1000$ ) is particularly interesting because many-dimensional data vectors allow high compression ratios.

Although the term replicator neural network is intended to apply to all autoassociative neural networks with compressed internal representations, for simplicity it will be used primarily in the following restricted sense. A replicator neural network is a multilayer perceptron with three hidden layers (see Fig. 1) that meets the following conditions [using the notation of (6)]: The input and output layers (layers 1 and 5) of this network each have  $m$  units. The inputs to layer 1 (the input layer) are the components of the data vector  $\mathbf{x}$  and the outputs of layer 5 are the components of  $\mathbf{x}'$  (intended to be an estimate of  $\mathbf{x}$ ). The output  $z_{ki}$  of unit  $i$  of layer  $k$  ( $k = 2, 3, 4$ , and 5) of the network is given by  $s_k(I_{ki})$ , where

$$I_{ki} = \sum_{j=0}^{L_k-1} w_{kij} z_{(k-1)j} \quad (1)$$

$w_{kij}$  is the weight of the  $i$ th unit of layer  $k$  that multiplies the output  $z_{(k-1)j}$  of unit  $j$  ( $j = 0, 1, \dots, L_k$ ) of the previous layer, and  $L_k$  is the number of units on layer  $k$ . The output of the  $i$ th unit of layer 1 (the input layer) is  $z_{1i} = x_i$  and the bias output  $z_{k0} = 1.0$  for  $k = 1, 2, 3$ , and 4. The activation functions  $s_k$  are given by  $s_2(\theta) = s_4(\theta) = \tanh(\theta)$  and  $s_3(\theta) = \theta$ . The activation function for the middle hidden layer is given by

$$s_3(\theta) = \frac{1}{2} + \frac{1}{2(N-1)} \sum_{j=1}^{N-1} \tanh \left[ a \left( \theta - \frac{j}{N} \right) \right] \quad (2)$$

This smooth staircase activation function with  $N$  treadles essentially quantizes the vector of middle hidden layer outputs into  $M = N^n$  grid points. As the staircase gain  $a \rightarrow \infty$  the middle hidden layer activation function approaches a discontinuous staircase function with exactly  $N$  output values:  $0, 1/(N-1), 2/(N-1), \dots, (N-2)/(N-1), 1$  (Fig. 2). If both  $a \rightarrow \infty$  and  $N \rightarrow \infty$ , then  $s_3(\theta)$  becomes the ramp activation function equal to 0 for  $\theta < 0$ ,  $\theta$  for  $0 \leq \theta \leq 1$ , and 1 for  $\theta > 1$ .

A real-time coder with  $M$  codes for a data vector source is a pair of mappings  $\alpha$  and  $\beta$ , with  $\alpha: A \subset \mathfrak{R}^m \rightarrow \{1, 2, \dots, M\}$  and  $\beta: \{1, 2, \dots, M\} \rightarrow \mathfrak{R}^m$ . The compression mapping  $\alpha$  maps each data vector  $\mathbf{x}$  to its code  $\alpha(\mathbf{x})$ , an integer between 1 and  $M$  [the inverse image  $\alpha^{-1}(i)$  of each code is assumed to be measurable]. The decompression mapping  $\beta(i)$  maps each code back to a data vector. The mean-squared-error distortion of this coder is

$$D = \int_A \|\mathbf{x} - \beta[\alpha(\mathbf{x})]\|^2 d\mu(\mathbf{x}) \quad (3)$$

Such a coder is optimal if it minimizes  $D$  in comparison with all other  $M$ -code coders for the same source. Clearly, in the high-gain case, replicator networks can be viewed as real-time coders with  $M = N^n$  codes.

Given any  $\epsilon > 0$ , it is straightforward to show that, for real-time coding, we can re-

HNC Software Inc., 5930 Cornerstone Court, San Diego, CA 92121, USA, and Department of Electrical and Computer Engineering and Institute for Neural Computation, University of California, San Diego, La Jolla, CA 92093, USA.